Imaging ion-molecule reactions: Charge transfer and halide transfer reactions of O^+ with CH_3Cl, CH_3Br, and CH_3I

Linsen Pei, James M. Farrar *

Department of Chemistry, University of Rochester, Rochester, NY 14627, USA

ABSTRACT

Velocity map images have been recorded for the charge transfer reactions of $O^+(^4S)$ with CH_3Cl, CH_3Br, and CH_3I at collision energies near 4 eV. The production of methyl halide cations occurs for all systems, with relative abundances ranging from 10 to 15% of the total reaction yield. In addition, small yields of the dissociative charge transfer products Br^+ and I^+ are observed. The velocity space images show that charge transfer is energy resonant, and occurs by long range electron transfer. The predominant product in all three systems is CH_3^+, which may form by dissociation of the nascent CH_3X^+ product on a quartet potential energy surface, or by halide ion abstraction from CH_3X by O^+ following a spin-changing transition from the initial quartet surface to a doublet surface. The kinetic energy distributions for CH_3^+ formation show both a sharp low energy feature that appears to describe the formation of $CH_3^+ + O$ $(^3P) + X(^2P)$, in addition to a higher energy component that describes the more exoergic channel forming $CH_3^+ + XO(^2\Pi)$. The relative intensity of this high energy feature increases as the halogen atom X changes from Cl to Br to I, a progression that correlates with the strength of the halogen atom spin–orbit splitting. This observation supports the conclusion that the formation of the CH_3^+ products via the most exoergic channels, i.e., $CH_3^+ + XO(^2\Pi)$, does occur through spin-changing collisions from quartet to doublet state surfaces that are mediated by spin–orbit coupling.

© 2014 Elsevier B.V. All rights reserved.

1. Introduction

The reactions of atomic oxygen cations have been the subject of many fundamental studies of gas phase ion chemistry. From the perspective of initiating a diverse range of chemical processes, the oxygen atomic cation is a particularly important species. With a recombination energy of 13.6 eV, charge transfer reactions occur with many stable atoms and molecules, often leading to subsequent dissociation and the production of energized fragments. The contributions of oxygen cation reactions in the F2 region of the ionosphere have been well-documented [1], as well as in the chemically complex environments of hydrocarbon flames [2] and semiconductor processing plasmas [3]. The reactivity of O^+ ions in the technologically important O_2/SiF_4 discharge employed in silicon etching is particularly well-established [4].

Despite the importance of this species in many chemical environments, studies of its chemistry with molecular systems are limited in number, both from the point of view of rates and reaction

dynamics. Reactions of O^+ with molecular hydrogen and its isotopomers have provided important examples of direct [5] and collision complex-mediated processes [6], have revealed the distinctive dynamical signature of sequential impulse interactions [7], and have demonstrated the value of molecular orbital and electronic state correlations in establishing reactive pathways in simple chemical systems [8,9]. Nevertheless, the scope of general reactivity patterns that O^+ exhibits with more complex collision partners remains quite limited.

Selected ion flow tube (SIFT) measurements of rates and branching ratios of O^+ with halogenated molecules at thermal energies are few in number but have revealed interesting reactivity patterns. The reactions of O^+ with methyl halides are of particular interest, given the significant atmospheric concentrations of these neutral species and their anthropogenic origins [10–12] . An early study by Mayhew et al. [13] of the $O^+ + CH_3Br$ system showed that CH_3^+ is the major product, but that the charge transfer products CH_3Br^+ and CH_2Br^+ represented approximately one-fourth of the total product yield. More recently, Nichols et al. [14] reported SIFT measurements of rates and branching ratios for O^+ reactions with a series of methyl halides and perfluorinated compounds. Consistent with Mayhew et al., this study confirmed that the dominant product with CH_3Br at thermal energies is CH_3^+, although no

* Corresponding author. Tel.: +1 585 275 5834; fax: +1 585 276 0205.
  E-mail addresses: linsen.pei@gmail.com (L. Pei), farrar@chem.rochester.edu
(J.M. Farrar).

evidence for the formation of CH_3Br^+ or CH_2Br^+ by charge transfer was found. This investigation confirmed that CH_3^+ is also the dominant product with CH_3Cl and CH_3I reactants, although C—O bond formation to produce HCO^+ and H_2CO^+ was reported with CH_3Cl, along with C—I bond cleavage in CH_3I to form I^+.

The dominance of the CH_3^+ product channel raises interesting questions concerning the role of electron spin: if CH_3^+ is formed by charge transfer followed by C—X bond cleavage, then it is accessible from the initially formed CH_3X^+ species without a change in spin. However, if CH_3^+ is formed by halide abstraction in concert with the production of a ground state XO radical, the system must cross from the initial quartet surface to a doublet surface. The experimental data reported in [14] did not allow a distinction between these two mechanisms for CH_3^+ formation. The authors reported the results of ab initio quantum chemical calculations on the CH_3Cl system on both doublet and quartet surfaces that rationalized the formation of CH_3^+ as well as reaction channels producing C—O bonds both on doublet and quartet surfaces.

Given the importance of the O^+ ion in the ionosphere, and the well-established presence in the atmosphere of methyl halides from anthropogenic sources, the rate determination is particularly significant. Experimental methods that provide dynamical information [15], such as energy and angular momentum partitioning and product angular distributions, complement rate measurements and have the capability to address questions that rate measurements cannot probe. In particular, velocity map ion imaging methods [16,17] have the potential to determine if CH_3^+ and X^+ products arise from unimolecular decay of the nascent parent ions or from spin-changing bimolecular collisions of the primary O^+ and CH_3X reactants.

In this study, we report velocity space imaging results for the reaction products of O^+ with the methyl halides CH_3Cl, CH_3Br, and CH_3I at hyperthermal collision energies near 4 eV. The distribution of reaction products at this collision energy, particularly the observation of non-dissociative charge transfer products, is significantly different from those reported at 300 K; however, the study confirms that CH_3^+ is the predominant reaction product at both energies. The velocity space images for the CH_3^+ products appear to provide insight into the mechanism of their formation.

The reactions we have addressed by velocity map imaging methods are listed below. The reactions include simple electron transfer, dissociative charge transfer to form halide cations, and the formation of CH_3^+ in concert with a bound or dissociated OX molecule.

$$O^+ + CH_3Cl \rightarrow CH_3Cl^+ + O \qquad \Delta H = -2.35 \text{ eV} \qquad (1)$$

$$\rightarrow CH_3^+ + Cl + O \qquad \Delta H = -0.16 \qquad (2)$$

$$\rightarrow CH_3^+ + ClO(^2\Pi) \qquad \Delta H = -2.95 \qquad (2a)$$

$$O^+ + CH_3Br \rightarrow CH_3Br^+ + O \qquad \Delta H = -3.07 \qquad (3)$$

$$\rightarrow CH_3^+ + Br + O \qquad \Delta H = -0.77 \qquad (4)$$

$$\rightarrow CH_3^+ + BrO(^2\Pi) \qquad \Delta H = -3.21 \qquad (4a)$$

$$\rightarrow Br^+ + CH_3 + O \qquad \Delta H = +1.20 \qquad (5)$$

$$O^+ + CH_3I \rightarrow CH_3I^+ + O \qquad \Delta H = -4.07 \qquad (6)$$

$$\rightarrow CH_3^+ + I + O \qquad \Delta H = -1.33 \qquad (7)$$

$$\rightarrow CH_3^+ + IO(^2\Pi) \qquad \Delta H = -7.37 \qquad (7a)$$

$$\rightarrow I^+ + CH_3 + O \qquad \Delta H = -0.69 \qquad (8)$$

Thermochemical data are from standard tabulations [18]. The large exoergicities for charge transfer reactions (1), (3), and (6), in conjunction with the collision energy are sufficient to drive the subsequent dissociation reactions. Although the lower ionization energy of CH_3 (9.84 eV) relative to the halogen atoms (11.82 eV and 10.45 eV for Br and I, respectively) suggests that CH_3^+ should be favored statistically by Stevenson's rule [19] in the subsequent dissociation of CH_3X^+ formed by charge transfer, the quantum chemical calculations suggest that CH_3^+ may also be formed by halide abstraction by O^+ from CH_3X. In the present study, the velocity map imaging method allows us to probe the dynamical signatures of the specific reaction motifs of charge transfer and subsequent dissociation processes, as well as the distinct dynamical behavior of possible halide transfer reactions.

2. Experimental

As described previously [20], the experiment is performed with a crossed beam instrument equipped with a velocity map imaging (VMI) detector [17]. The imaging system measures all product velocities for a given mass in a single detection time interval. Detecting products at variable delay times after extracting products from the collision region allows products of different masses to be imaged. The experimental method is similar to schemes employed in other laboratories [21–26].

The primary ion beam is formed by electron impact [27] on a mixture of 10% CO in He. The primary product of electron impact on this mixture is He^+, which then undergoes charge transfer with CO to form both parent and fragment C^+ and O^+ cations. As discussed by Smith et al. [28], the production of CO^+ by charge transfer of CO with O^+ is endoergic for ground state cations, but is exoergic for the ^2S and ^2D excited states. In a crossed beam geometry in which the O^+ ion beam intersected a CO beam, we were unable to detect CO^+ cations. This observation places a limit on excited state $O^+(^2D, ^2P)$ production of less than 1%.

Ions produced by electron impact are extracted, mass selected, and decelerated and focused by a series of ion optics, and the continuous beam of ions is delivered to the volume defined by the repeller and extraction electrodes of a velocity map imaging detector. The ion beam has a roughly triangular kinetic energy distribution with a FWHM of approximately 0.20 eV in the laboratory frame of reference. The neutral beam is produced by a pulsed solenoid valve located 10 mm upstream from a 1 mm skimmer. For the production of beams of CH_3Cl and CH_3Br, the neat gas from a lecture bottle cooled to 0 °C produced stagnation pressures behind the 0.1 mm diameter nozzle of 2.6 and 0.9 atm, respectively. For the production of CH_3I beams, liquid CH_3I cooled to 0 °C was seeded in He carrier gas at a backing pressure of ~1 atm. The pressure in the collision chamber was ~1×10^{-6} torr with the beams running.

As described previously [20], resonant charge transfer between an ion beam of Ar^+ and a neutral beam of Ar produced by supersonic expansion is employed to establish a velocity marker at thermal velocity, corresponding to a lab energy of 0.064 eV. Coupled with direct measurement of the ion beam energy distribution with an electrostatic energy analyzer, these measurements result in a velocity scale that is accurate to $\pm 0.2 \times 10^2$ m s^{-1}.

Although the beam energy spreads make a significant contribution to the overall detector resolution, the primary experimental contribution comes from the finite thickness of the collision center. Reaction products formed at various depths

within the collision volume are accelerated to different extents and therefore do not satisfy a unique velocity-mapping condition.

3. Results and discussion

3.1. General dynamical signatures: velocity map images

In this presentation of the experimental results, we first focus on the general shapes of the velocity space images and the qualitative dynamical classifications that these images reveal.

3.1.1. Charge transfer

In contrast to the thermal energy flow tube results, the hyperthermal crossed beam experiments provide direct evidence for the formation of methyl halide cations by charge transfer, with relative abundances ranging from 10 to 15%. The relative intensity data are summarized in Table 1. Fig. 1 shows the images for CH_3Cl^+, CH_3Br^+, and CH_3I^+ product formation superimposed on the Newton diagrams describing the directions of the ion and neutral beam velocity vectors and the centroid vectors $\boldsymbol{C}$, all referenced to the laboratory origin. The circles denote the locus of points corresponding to the maximum values of the center of mass speeds for the charge transfer products allowed by energy conservation. The images show that the charge transfer products appear near the tip of the neutral velocity vector, and follow the locus expected for elastic scattering of the reaction products in the exit channel. This behavior is precisely what is expected for energy resonant charge transfer, in which the kinetic energies of the molecular precursors and the charge transfer products are unchanged.

The experimental images are Cartesian representations of product ion flux as a function of laboratory velocity $\boldsymbol{v}$, where laboratory velocity vectors are referred to the lab coordinate origin defined by the crossing point of the beams [29,30]. The velocity vector of the center of mass of the collision partners is denoted by $\boldsymbol{C}$, and the relationship between laboratory velocity vectors $\boldsymbol{v}$ and their corresponding values $\boldsymbol{u}$ in center of mass coordinates is given by a simple velocity shift [31]:

$$\boldsymbol{u} = \boldsymbol{v} - \boldsymbol{C} \tag{9}$$

Because the velocity map imaging detection scheme intrinsically recovers intensity in Cartesian coordinates, the transformation from laboratory coordinates to barycentric flux distributions in Cartesian coordinates, symbolized by $P(\boldsymbol{u}_x, \boldsymbol{u}_y)$, is straightforward [30]. Recoil speed and scattering angle in center of mass coordinates are given by the following expressions:

$$\boldsymbol{u} = (\boldsymbol{u}_x^2 + \boldsymbol{u}_y^2)^{1/2} \tag{10}$$

$$\theta = \tan^{-1}\left(\frac{\boldsymbol{u}_y}{\boldsymbol{u}_x}\right) \tag{11}$$

Table 1
Product branching ratios.

Reactants	Products	Branching fraction (this work)	Branching fraction (Ref. [10])
$O^+ + CH_3Cl$	CH_3Cl^+	0.1 ± 0.02	0
	CH_3^+	0.9 ± 0.02	0.88
	HCO^+, H_2CO^+	0	0.12
$O^+ + CH_3Br$	CH_3Br^+	0.09 ± 0.02	0
	CH_3^+	0.89 ± 0.02	1
	Br^+	0.02 ± 0.01	0
$O^+ + CH_3I$	CH_3I^+	0.15 ± 0.02	0
	CH_3^+	0.64 ± 0.02	0.94
	I^+	0.21 ± 0.02	0.06
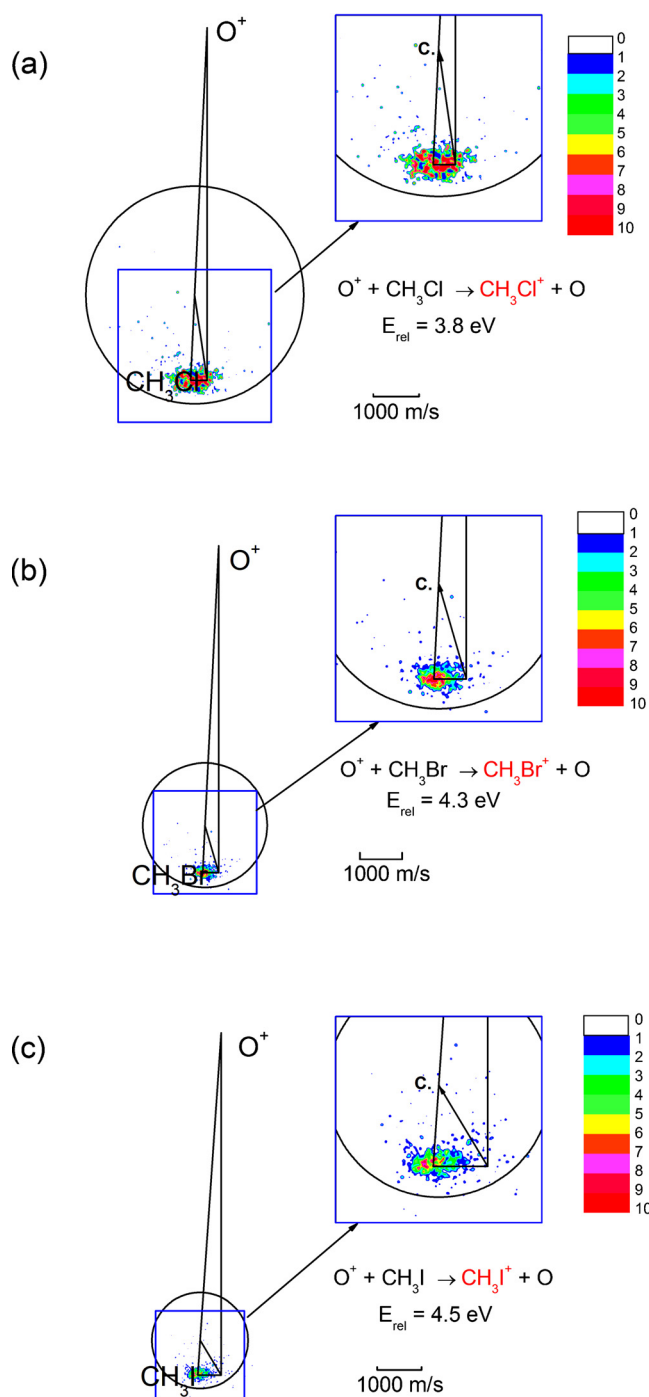
Fig. 1. Velocity map images for charge transfer. (a) CH_3Cl^+, (b) CH_3Br^+, (c) CH_3I^+. Relative energies for each system indicated. As shown in the inset, the direction of the center of mass of the system is indicated by $\boldsymbol{C}$. The relative flux intensities are indicated by the color bar scale shown in the figure. The circles denote the maximum product speeds allowed by the energies available to reaction products.

By integration of the velocity space images over scattering angle according to Eq. (12),

$$\langle P(E_T') \rangle_\theta = \int_0^\pi d\theta \; \sin\theta \; \boldsymbol{u} \; P(\boldsymbol{u}_x, \boldsymbol{u}_y) \tag{12}$$

the product kinetic energy distribution for charge transfer may be obtained, and these results are shown in the top panel of Fig. 2. Immediately obvious is the fact that the distributions peak at the collision energy of the experiments, indicative of energy resonant
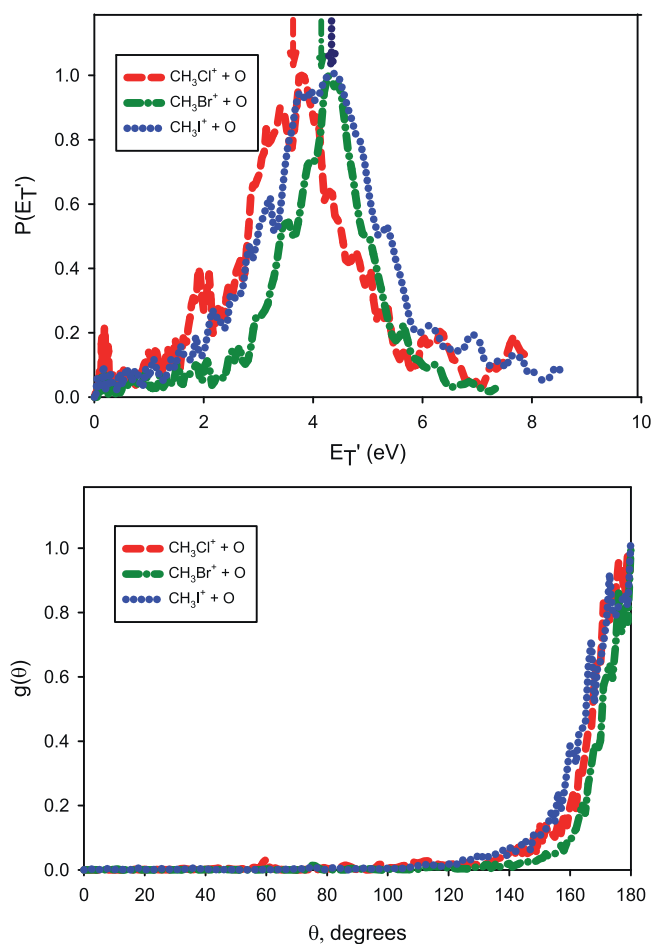
Fig. 2. Top panel: kinetic energy distributions $P(E'_T)$ for formation of CH_3Cl^+, CH_3Br^+, and CH_3I^+. Vertical arrows denote mean collision energies for the corresponding distributions. Bottom panel: product angular distributions $g(\theta)$ for formation of CH_3Cl^+, CH_3Br^+, and CH_3I^+.

charge transfer in which the kinetic energies of the reactants and products are equal. As noted in our other publications [20,32,33], the kinetic energy distributions in charge transfer mirror the distributions of internal states consistent with the Franck–Condon factors connecting the neutral reactant and its ion [34,35]. The low energy photoelectron spectra of methyl halides provide some insight on this point: the spectra generally show a weakly structured band near threshold, consistent with Franck–Condon activity in the C—X stretch of the methyl halide [36].The product angular distributions obtained by integrating the velocity space distributions over recoil speed may be calculated according to Eq. (13),

$$\langle g(\theta) \rangle_{\boldsymbol{u}} = \int_0^\infty d\boldsymbol{u} \ \boldsymbol{u}^2 P(\boldsymbol{u}_x, \boldsymbol{u}_y) \qquad (13)$$

and as shown in the bottom panel of Fig. 2, are sharply peaked at 180° in the center of mass system, consistent with the negligible change in momentum of the methyl halide cation relative to its neutral precursor. Energy and angular distributions like those shown in Fig. 2 are a signature of long range resonant charge transfer.

3.1.2. Dissociative charge transfer: Br+ and I+ formation

The mass resolution of the imaging method precludes the measurement of images resulting from hydrogen atom loss from nascent methyl halide cations formed by direct charge transfer.

However, methyl halide cations may also dissociate to the methyl cation and a halogen atom, or to a halogen cation and a methyl radical. The lower ionization energy of CH_3 relative to the halogen atoms makes the former the favored dissociation product. At the thermal energies of the flow tube experiments, only cleavage of the weak C—I bond occurs to produce I+ [14]. However, at the hyperthermal collision energies of the present experiments, the reaction thermochemistry allows both Br+ and I+ to be formed from CH_3Br and CH_3I, respectively. The velocity space images for these products are shown in Fig. 3. As was the case with the methyl halide cations, the images show that the products are also centered on the tip of corresponding neutral beam vectors, and support the claim that these species are formed by dissociative ionization of the methyl halide.

The product relative translational energy of the three-body systems $X^+ + CH_3 + O$ is given as the sum of the relative translational energy between O and the center of mass of the fragments $CH_3 + X^+$, plus the relative translational energy of the separating fragments. We expect the $CH_3 + X^+$ products to follow the velocity vector of the precursor methyl halide cation product. Although the Br+ and I+ images are perceptibly broader than those associated with the methyl halide products, they are reasonably sharp, and justify an
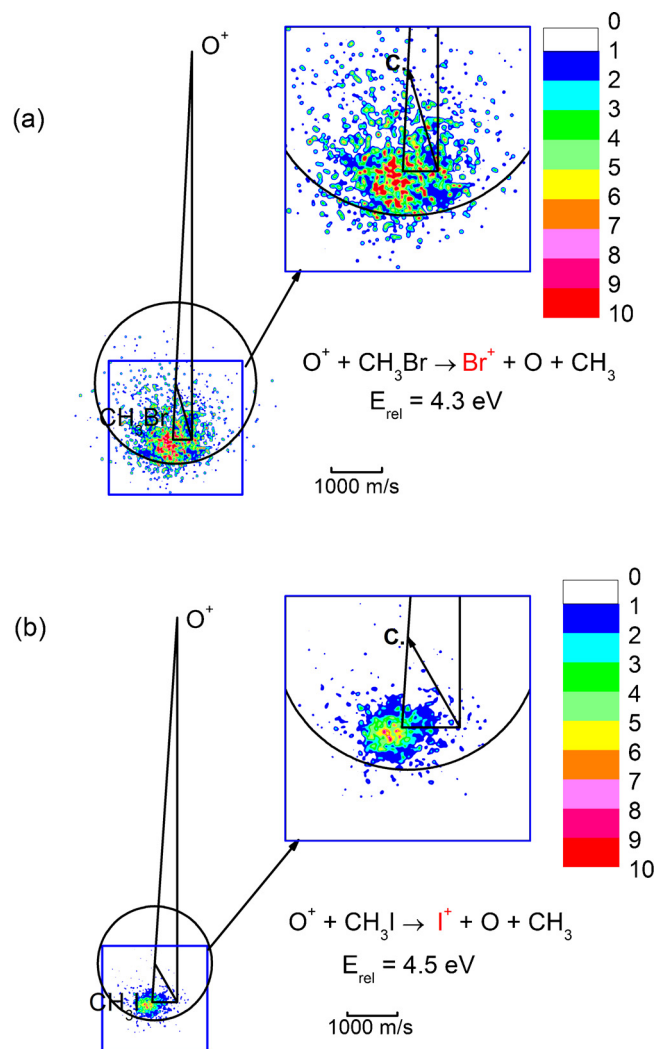
Fig. 3. Velocity map images for dissociative charge transfer. (a) Br+, (b) I+. Relative energies for each system indicated. The direction of the center of mass of the system is indicated by **C**. The relative flux intensities are indicated by the color bar scale shown in the figure. The circles denote the maximum product speeds allowed by the energies available to reaction products.
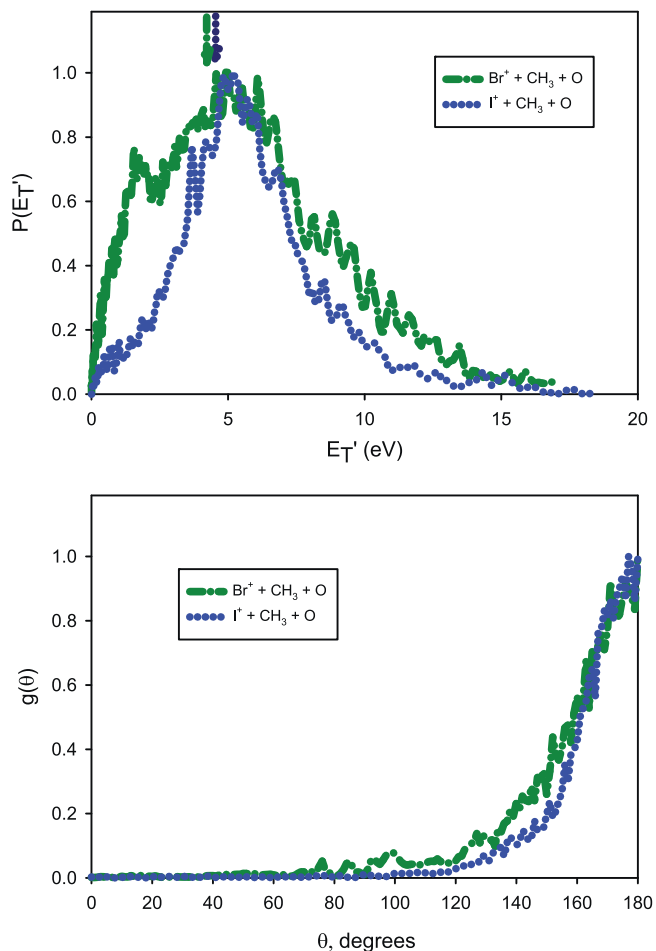
analysis based on the collision-activated dissociation of polyatomic ions [37–39]. This method sets the center of mass velocity vector $\boldsymbol{u}$ for the detected product Br^+ or I^+ equal to the CH_3Br^+ or CH_3I^+ velocity determined by momentum matching to the accompanying O atom product, i.e., $|\boldsymbol{u}| = \boldsymbol{u}_{X^+} \approx \boldsymbol{u}_{CH_3X^+}$. The final relative translational energy of the products is computed from the center of mass speed of the detected fragment through the relationship

$$E'_T = \frac{1}{2}\frac{m_{CH_3X}}{m_O}M\boldsymbol{u}^2 \qquad (14)$$

where M is the total mass of the collision system and $\boldsymbol{u}$ is the center of mass speed of the detected fragment ion.

The results of this approximate kinematic analysis may be employed to produce product kinetic energy distributions and angular distributions for the Br^+ and I^+ products and are shown in Fig. 4. The similarities of these plots to the kinetic energy and angular distributions for the primary methyl halide products in Fig. 2 provide reasonable confirmation that these halogen cation products are the result of dissociative charge transfer. Perhaps a subtle distinction, the picture of dissociative charge transfer that emerges from the data is that the process occurs as the primary charge transfer product CH_3X^+ undergoes C—X bond cleavage to form $CH_3 + X^+$, rather than by a single step collision-induced dissociation process.

3.1.3. CH_3^+ formation

The crossed beam studies show that the formation of CH_3^+ is the dominant reaction process, ranging from 64% of the total product yield for CH_3I to ~90% for CH_3Br and CH_3Cl. Although the relative intensities of the CH_3^+ products in the hyperthermal energy range of the present experiments are quantitatively different than the results at 300 K, this product is the dominant one in both energy regimes. The results are shown in Table 1.

Based on prior observations that the products of dissociative charge transfer have energy distributions that mimic those of the parent ions [33], a comparison of the velocity space images for CH_3^+ formation with those of the CH_3X^+ precursors is instructive. Those images are shown in Fig. 5, and the comparison is quite striking. The CH_3^+ images cover a much broader region of velocity space than those for CH_3X, and are not centered on the tip of the neutral beam velocity vector as would be expected for products formed by

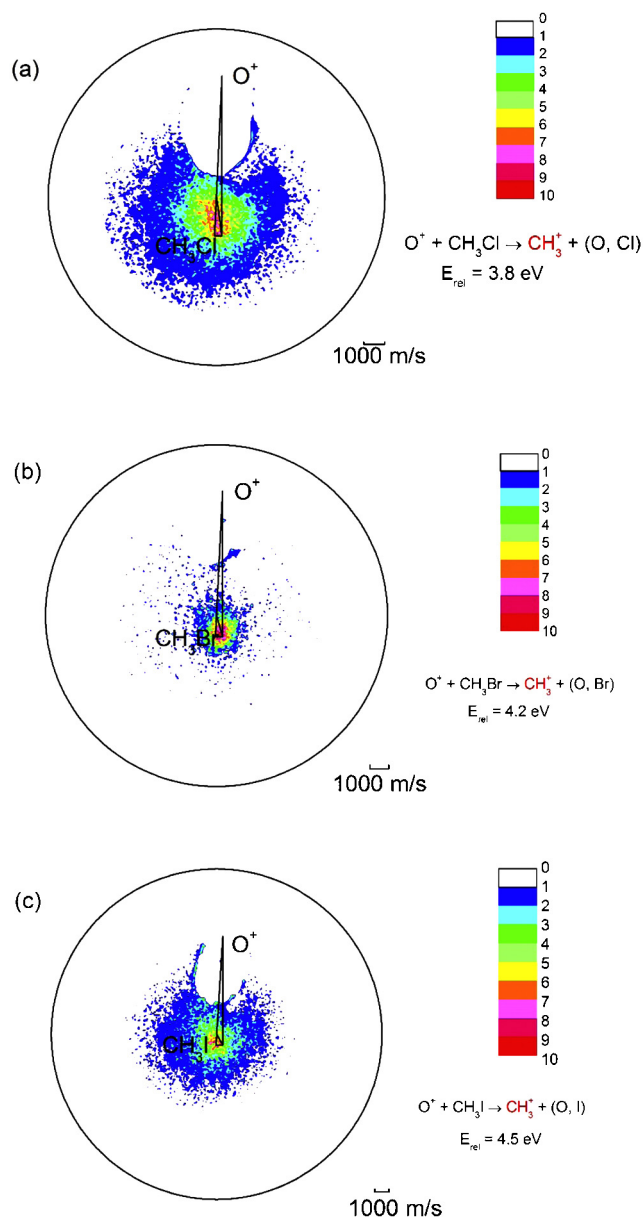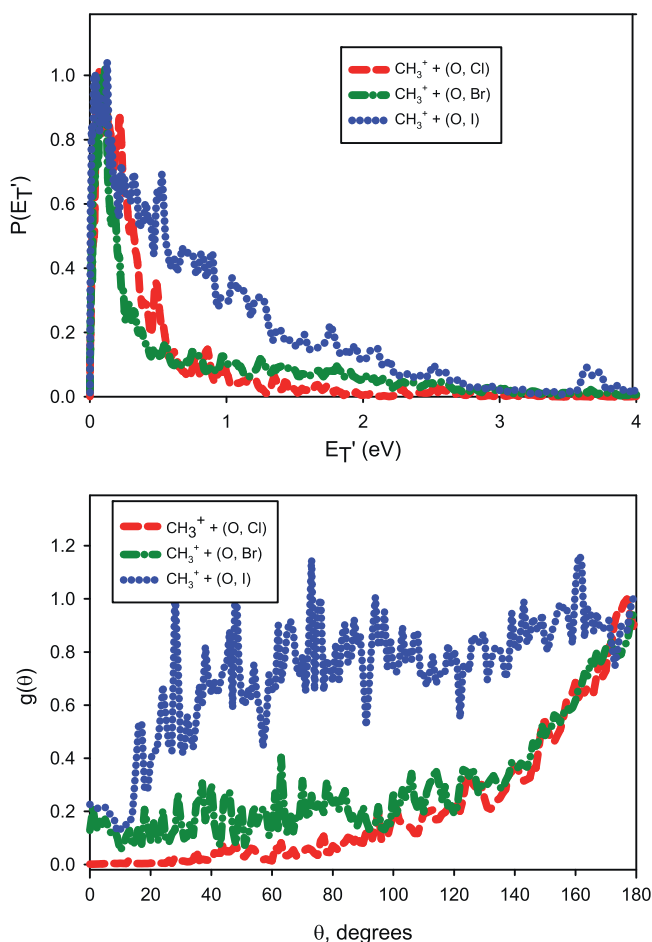
Fig. 4. Top panel: kinetic energy distributions $P(E'_T)$ for formation of Br^+ and I^+. Vertical arrows denote mean collision energies for the corresponding distributions. Bottom panel: product angular distributions $g(\theta)$ for formation of Br^+ and I^+.

Fig. 5. Velocity map images for CH_3^+ formation charge transfer. (a) from CH_3Cl, (b) from CH_3Br, (c) from CH_3I. Relative energies for each system indicated. The relative flux intensities are indicated by the color bar scale shown in the figure. The circles denote the maximum product speeds allowed by the energies available to reaction products.

Fig. 6. Top panel: kinetic energy distributions $P(E'_T)$ for formation of CH_3^+ from CH_3Cl, CH_3Br, and CH_3I. Bottom panel: product angular distributions $g(\theta)$ for formation of CH_3^+ from CH_3Cl, CH_3Br, and CH_3I.

dissociative charge transfer, but instead are centered on the relative velocity vector and are displaced toward the system centroid.

A closer look at the product kinetic energy and angular distributions provides more insight into the dynamical implications of these clear deviations from the dissociative charge transfer picture. In the top panel of Fig. 6, we plot the kinetic energy distributions for CH_3^+ formation from CH_3Cl, CH_3Br, and CH_3I. The energies available to these reaction products correspond to the sum of collision energy, approximately 4 eV in each case, and the reaction ΔH values, and are significantly larger than the maximum values of the kinetic energies that are observed. In the CH_3Cl case, the kinetic energy distribution consists of a single dominant peak at low energy, and a weak tail that extends out to ~2 eV. There is negligible product intensity beyond 2 eV. In contrast to the kinetic energy release for CH_3^+ from CH_3Cl, the energy distribution for CH_3^+ from CH_3Br shows a low energy peak but also a very broad tail that extends out to beyond 3 eV, suggestive of a two channel decay mechanism. The product intensity in this tail is approximately one-quarter of the total product intensity. The kinetic energy distribution of CH_3^+ from CH_3I rises rapidly from zero and has a very significant tail to high energy that extends to 3 eV and dominates the distribution. Approximately 75% of the CH_3^+ flux appears in this tail.

Although the mass ratio of the CH_3^+ product relative to the momentum-matched (O, X) fragments decreases as the halogen mass increases, the kinematic resolution of the experiment is not affected by this small velocity space compression. The two-component character of the energy distributions is not a kinematic artifact. Integration of the velocity space distributions with Eq. (12)

separately over the angular ranges $0 \le \theta \le 90°$ (forward hemisphere) and $90° \le \theta \le 180°$ (backward hemisphere) shows that the broad high energy feature is angle independent, while the sharp low energy peak appears to be concentrated in the forward hemisphere. Both of these observations support the conclusion that two separate pathways produce CH_3^+, and a consideration of the features of the doublet and quartet potential energy surfaces is necessary to provide additional insight into those pathways.

The angular distributions for CH_3^+ formation, obtained by integrating the velocity space flux distributions over recoil speed according to Eq. (13), are shown in the bottom panel of Fig. 6, and indicate that the products are distributed over a broad angular range. The distributions for $CH_3^+ + (O, Cl)$ and $CH_3^+ + (O, Br)$ products, where the (O, X) notation represents both bound and unbound XO products, are similar, exhibiting backward scattered peaks reminiscent of the distributions that characterize charge transfer, but are significantly broader. The (O, Br) distribution has a significant component that extends into the forward hemisphere. Particularly interesting is the angular distribution for the $CH_3^+ + (O, I)$ products, which displays a plateau that falls off very slowly from its maximum value at $180°$ and extends well into the forward direction. This angular distribution is consistent with product formation occurring on a timescale comparable to the rotational period of the CH_3OI^+ adduct [40].

The energy and angular distributions for CH_3^+ formation suggest that more than one collision pathway is implicated in the formation of this species. As noted previously by Nichols et al. [14], a consideration of electron spin shows that the production of CH_3^+ by simple bond cleavage of the C—X bond in the methyl halide cation to form $CH_3^+ + X + O$ products is spin-allowed. In contrast, the two-body reactions between $O^+(^4S)$ and CH_3X to form $CH_3^+ + OX$ $(X^2\Pi)$ by halide abstraction, reactions (4a) and (7a), are spin-forbidden and are thus affected strongly by the identity of the halogen atom in CH_3X. The energy accessible to CH_3^+ and the dissociated OX molecule via a spin-allowed pathway is clearly less than that available for CH_3^+ formed in concert with a bound OX molecule via a spin-forbidden path. Consequently, the strong effect of halogen identity on the intensity of the high energy component of the CH_3^+ velocity distributions is consistent with the claim that a significant fraction of those products are formed along a pathway in which reactants evolving initially on a quartet surface undergo a transition to a doublet state facilitated by spin–orbit coupling.

3.2. Potential energy surfaces

The quantum chemical calculations reported by Nichols et al. [14] provide a useful starting point for understanding the relative energetics of reactive intermediates on the doublet and quartet surfaces in the $O^+ + CH_3X$ systems. These calculations, carried out on the CH_3Cl system at the CCSD(T)/aug-cc-pVDZ level of theory, are qualitative only, but do provide insight into reaction pathways on surfaces of different multiplicities, and the general relationships among reactants, products, and intermediates can be extended to the $O^+ + CH_3Br$ and CH_3I systems. Because the calculations do not reproduce known energetics for enthalpies of formation for the reaction products or excited state reactants, we use tabulated thermochemical data [18] in conjunction with the calculations to produce a reaction coordinate diagram. The principal objective of constructing this diagram is to understand the role that spin-changing collisions play in directing the distinct pathways for the formation of the dominant reaction product, CH_3^+.

The qualitative reaction coordinate diagram for the $O^+ + CH_3Cl$ system is shown in Fig. 7. Approach of the $O^+(^4S)$ reactant to CH_3Cl leads to ground state charge transfer products $O(^3P) + CH_3Cl^+$ lying 2.36 eV below the reactants. Standard thermochemical data [18] show that the dissociation of the C—Cl bond in CH_3Cl^+ to form singlet state $^1CH_3^+ + Cl(^2P)$ requires 2.19 eV. Fig. 7 thus indicates that the
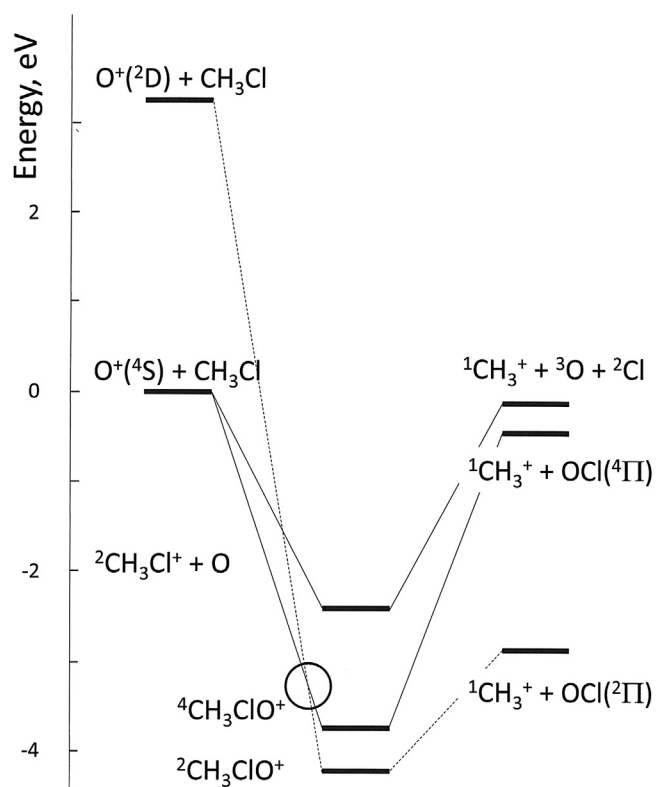
Fig. 7. Schematic reaction coordinate for the $O^+ + CH_3Cl$ system. Energies for $O^+(^4S, ^2D)$, CH_3Cl, singlet state CH_3^+, $ClO(^2\Pi)$, $O(^3P)$, and $Cl(^2P)$ are from standard thermodynamic data [17]. Energies of $^{2,4}CH_3ClO^+$ adducts and $ClO(^4\Pi)$ are computed values from Ref. [10]. A circle denotes the quartet–doublet surface crossing.

formation of $^1CH_3^+ + O(^3P) + Cl(^2P)$ occurs on a single potential energy surface of quartet multiplicity. Similarly, the quartet state CH_3OCl^+ adduct accessible from the ground state reactants lying nearly 3 eV below the reactants may dissociate to $CH_3^+ + ClO(^4\Pi)$.

Fig. 7 also shows the same quartet-doublet interaction reported in [14] that mediates spin-changing collisions in the entrance channel. Such collisions provide access to a doublet state adduct of CH_3OCl^+, which serves a precursor to halide abstraction by O^+ from the CH_3Cl reactant to form $^1CH_3^+ + ClO(^2\Pi)$. Fig. 7 shows clearly that reactive collisions evolving initially on the quartet surface generated by the approach of $O^+(^4S)$ to CH_3Cl may cross to a doublet state originating from the $O^+(^2D)$ excited state reactants. This surface leads to a doublet CH_3ClO^+ intermediate that forms the halide ion abstraction products $^1CH_3^+ + ClO(^2\Pi)$.

The structure of the energy level diagram of reactants, products, and intermediates differs in detail for CH_3Br and CH_3I reactants, but has the same general appearance. The important feature relevant to the kinetic energy distributions that characterize $^1CH_3^+$ formation is that the relative contribution to the highest kinetic energy component of the distribution is controlled by the spin–orbit interaction that directs collisions to doublet state CH_3XO^+ intermediates. Similarly, low recoil energy CH_3^+ products formed in concert with $Cl(^2P)$ and $O(^3P)$ atomic products may remain on the initial quartet surface. The experimental data presented in this paper for CH_3^+ formation are consistent with this picture.

4. Conclusions

Crossed beam studies of the chemical reactions displayed by ground state $O^+(^4S)$ with the methyl halides CH_3Cl, CH_3Br, and CH_3I have provided dynamical insights into these important systems for which rate and branching ratios at room temperature have been

reported only recently [14]. Velocity map imaging studies of energy disposal for charge transfer have shown that long range electron transfer is responsible for the production of methyl halide cations, with the products exhibiting the velocity space motif typical for the process. Formation of Br^+ and I^+ exhibit the same motif, therefore establishing their production as a dissociative charge transfer process.

Measurement of product kinetic energy distributions for CH_3^+ formation have established that there are two routes to this product: in the first, CH_3^+ is formed by C—X bond cleavage in the nascent CH_3X^+ charge transfer product. This process occurs without a change in spin. The second route forms products with significantly larger kinetic energy release, consistent with their formation in concert with a bound XO molecular product. The systematic increase in intensity of this feature in the kinetic energy distributions as the halogen varies from chlorine to bromine to iodine supports the claim that the second mechanism for CH_3^+ formation proceeds by halide abstraction on a doublet potential energy surface, requiring a spin-changing collision facilitated by spin–orbit coupling.

The chemistry of the O^+ cation is diverse, with the potential to reveal many interesting lessons about chemical reaction dynamics. We look forward to additional contributions in this important area of gas phase ion chemistry.

Acknowledgements

References

[1] E.E. Ferguson, F. Arnold, Acc. Chem. Res. 14 (1981) 327.
[2] J.M. Goodings, D.K. Bohme, C.W. Ng, Combust. Flame 36 (1979) 27.
[3] P.B. Armentrout, Adv. At. Mol. Opt. Phys. 43 (2000) 187.
[4] E.R. Fisher, P.B. Armentrout, J. Phys. Chem. 95 (1991) 6118.
[5] K.T. Gillen, B.H. Mahan, J.S. Winn, J. Chem. Phys. 59 (1973) 6380.
[6] K.T. Gillen, B.H. Mahan, J.S. Winn, J. Chem. Phys. 58 (1973) 5373.
[7] K.T. Gillen, B.H. Mahan, J.S. Winn, Chem. Phys. Lett. 22 (1973) 344.
[8] B.H. Mahan, J. Chem. Phys. 55 (1971) 1436.
[9] B.H. Mahan, Acc. Chem. Res. 8 (1975) 55.
[10] E. Blei, M.R. Heal, Atmos. Environ. 45 (2011) 1543.
[11] K.R. Redeker, N.Y. Wang, J.C. Low, A. McMillan, S.C. Tyler, R.J. Cicerone, Science 290 (2000) 966.
[12] R.C. Rhew, J. Geophys. Res. Biogeosci. 116 (2011).
[13] C.A. Mayhew, R. Thomas, P. Watts, Int. J. Mass Spectrom. 223 (2003) 91.
[14] C.M. Nichols, Z.B. Yang, B.B. Worker, D.R. Hager, N.M.M. Nibbering, V.M. Bierbaum, Phys. Chem. Chem. Phys. 15 (2013) 561.
[15] J.M. Farrar, in: J.M. Farrar, W.H. Saunders Jr (Eds.), Techniques for the Study of Ion–Molecule Reactions, Wiley, New York, 1988, pp. 325.
[16] A.G. Suits, R.E. Continetti (Eds.), Imaging in Chemical Dynamics, American Chemical Society, Washington D.C, 2001.
[17] A. Eppink, D.H. Parker, Rev. Sci. Instrum. 68 (1997) 3477.
[18] S.G. Lias, NIST chemistry WebBook, in: P.J. Linstrom, W.G. Mallard (Eds.), NIST Standard Reference Database No. 69, National Institute of Standards and Technology, Gaithersburg, M.D, 2005.
[19] D.P. Stevenson, Disc. Faraday Soc. (1951) 35.
[20] L. Pei, J.M. Farrar, J. Chem. Phys. 136 (2012) 204305.
[21] E.L. Reichert, S.S. Yi, J.C. Weisshaar, Int. J. Mass Spectrom. 196 (2000) 55.
[22] E.L. Reichert, G. Thurau, J.C. Weisshaar, J. Chem. Phys. 117 (2002) 653.
[23] E.L. Reichert, J.C. Weisshaar, J. Phys. Chem. A 106 (2002) 5563.
[24] J. Mikosch, U. Fruhling, S. Trippel, D. Schwalm, M. Weidemuller, R. Wester, Phys. Chem. Chem. Phys. 8 (2006) 2990.
[25] J. Mikosch, S. Trippel, C. Eichhorn, R. Otto, U. Lourderaj, J.X. Zhang, W.L. Hase, M. Weidemuller, R. Wester, Science 319 (2008) 183.
[26] J.X. Zhang, J. Mikosch, S. Trippel, R. Otto, M. Weidemuller, R. Wester, W.L. Hase, J. Phys. Chem. Lett. 1 (2010) 2747.
[27] H. Udseth, C.F. Giese, W.R. Gentry, Phys. Rev. A 8 (1973) 2483.
[28] D. Smith, P. Spanel, C.A. Mayhew, Int. J. Mass Spectrom. Ion Process. 117 (1992) 457.
[29] R. Wolfgang, R.J. Cross, J. Phys. Chem. 73 (1969) 743.
[30] B. Friedrich, Z. Herman, Collect. Czech. Chem. Commun. 49 (1984) 570.
[31] J.M. Farrar, in: P.B. Armentrout (Ed.), The Encyclopedia of Mass Spectrometry, Elsevier, Amsterdam, 2003, pp. 158.
[32] L. Pei, J.M. Farrar, J. Chem. Phys. 137 (2012) 154312.
[33] L. Pei, J.M. Farrar, J. Chem. Phys. 138 (2013) 124304.

[34] V.G. Anicich, J.B. Laudenslager, W.T. Huntress, J.H. Futrell, J. Chem. Phys. 67 (1977) 4340.

[35] J.B. Laudenslager, W.T. Huntress, M.T. Bowers, J. Chem. Phys. 61 (1974) 4600.

[36] D.W. Turner, Phil. Trans. R. Soc. A 268 (1970) 7.

[37] Z. Herman, J.H. Futrell, B. Friedrich, Int. J. Mass Spectrom. Ion Process. 58 (1984) 181.

[38] A.K. Shukla, K.G. Qian, S.L. Howard, S.G. Anderson, K.W. Sohlberg, J.H. Futrell, Int. J. Mass Spectrom. Ion Process. 92 (1989) 147.

[39] A.K. Shukla, K. Qian, S. Anderson, J.H. Futrell, J. Am. Soc. Mass Spectrom. 1 (1990) 6.

[40] M.K. Bullitt, C.H. Fisher, J.L. Kinsey, J. Chem. Phys. 60 (1974) 478.